Appl Phys B (2010) 101: 761–771
DOI 10.1007/s00340-010-4100-0

Applied Physics B
Lasers and Optics

X-ray generation from slanting laser–Compton scattering for future energy-tunable Shanghai Laser Electron Gamma Source

W. Luo · W. Xu · Q.Y. Pan · X.Z. Cai · Y.Z. Chen · G.T. Fan · G.W. Fan · Y.J. Li · W.H. Liu · G.Q. Lin · Y.G. Ma · W.Q. Shen · X.C. Shi · B.J. Xu · J.Q. Xu · Y. Xu · H.O. Zhang · Z. Yan · L.F. Yang · M.H. Zhao

Received: 7 March 2010 / Revised version: 21 May 2010 / Published online: 23 June 2010

Abstract There is great interest in the generation of energy-tunable, bright, short-pulse X/γ-ray sources, which are required in various research fields. Laser–Compton scattering (LCS) is considered to be one of the most promising methods to implement this kind of X/γ-ray source. At the 100-MeV LINAC of the Shanghai Institute of Applied Physics, a 2-J, 8-ns, 1064-nm, Q-switched Nd:YAG laser is brought to a slanting collision at 40° (44°) with an 112-MeV, 0.9-ns (rms) relativistic electron beam. We measured the LCS X-ray energy spectrum with a peak energy of $31.73 \pm 0.22_{\text{stat}} \pm 1.64_{\text{syst}}$ keV and a peak width (rms) of $0.74 \pm 0.26_{\text{stat}} \pm 0.03_{\text{syst}}$ keV. This preliminary investigation was carried out to understand the feasibility of developing an energy-tunable X/γ-ray source. Based on this study, the future Shanghai Laser Electron Gamma Source (SLEGS) at the Shanghai Synchrotron Radiation Facility (SSRF) can be constructed to be not only an energy-tunable γ-ray source by guiding the laser incident angle from laser–Compton scattering, but also a high flux ($\sim 10^{10}$ photons/s or even higher) γ-ray source by adding a laser super-cavity.

W. Luo · W. Xu (✉) · Q.Y. Pan · X.Z. Cai · Y.Z. Chen · G.T. Fan · G.W. Fan · Y.J. Li · W.H. Liu · G.Q. Lin · Y.G. Ma · W.Q. Shen · B.J. Xu · J.Q. Xu · Y. Xu · H.O. Zhang · Z. Yan · L.F. Yang · M.H. Zhao
Shanghai Institute of Applied Physics, Chinese Academy of Sciences, Shanghai 201800, China
e-mail: wangxu@sinap.ac.cn

X.C. Shi
Shanghai Institute of Optics and Fine Mechanics, Chinese Academy of Sciences, Shanghai 201800, China

W. Luo · G.T. Fan · G.W. Fan · Y.J. Li · Y. Xu · L.F. Yang
Graduate School of the Chinese Academy of Sciences, Beijing 100039, China

1 Introduction

During the last few decades, the rapid development of electron accelerator and laser techniques such as third-generation synchrotron radiation facilities, chirped-pulse amplification techniques, and the significant improvement of synchronization between high-brightness electron beams and high-intensity lasers has opened new possibilities for the generation of short-pulse and high to moderate-flux X/γ-ray sources. These X/γ-ray sources are required in various research fields, such as material, chemical, medical and biological sciences.

One of the most promising approaches to short-pulse and high to moderate-flux X/γ-ray generation is the use of the laser-Compton scattering (LCS). Compton scattering of a relativistic electron beam from a laser is proven to be an effective technique to generate high-brightness X/γ-rays [1–9]. LCS X/γ-ray sources can possess unprecedented compactness, brilliance, energy tunability, monochromaticity and pulse speeds, with radiation pulse durations in the ps to fs range and fluxes of 10^{11} photons/s and higher within a small energy bandwidth.

Other X-ray sources like X-ray laser, synchrotron, and free-electron laser light sources are also popular. X-ray lasers, such as those based on laser-produced plasma (LPP) and discharge-produced plasma (DPP), are bright and can be of tabletop size, but are not tunable [10, 11]. Free-electron lasers and synchrotron radiation sources are large installations for generating X-rays but cannot produce the harder photons made by LCS X-ray sources. LCS are candidates not only for X-ray sources, but also for γ-ray sources, which can be used for nuclear physics, astrophysics, nuclear data, and nuclear structure studies [12–17], and high-energy physics applications, e.g. production of polarized positron beams for future positron injectors, and photon linear colliders (γ–γ, γ–lepton, e^+/e^- colliders) [18–24].

In addition, LCS sources are playing an increasingly critical role for some other research applications. These applications include:

- Medical and biological imaging (e.g. X-ray absorption imaging, refraction contrast imaging and angiography) [25–30].
- Solid-state physics and material sciences.
- Radiation detector development (e.g. X-ray line sensor for American Homeland security) [31].
- Radioactive isotopes detection (e.g. non-destructive detection and assay of radioactive isotopes in various materials which are essential for enabling nuclear power to emerge as a sustainable and secure source of primary energy, segregation of nuclear waste, and standoff detection of clandestine fissile material in cargo and packages, which is indispensable for advanced safeguarding and non-proliferation in the nuclear power systems) [32–35].
- ps or fs X-ray microscopy and holography, dynamic analysis of chemical reactions, phase transitions, and other ultrafast processes traced to atomic precision [8, 36–39].
- Cancer therapy by a high-energy photon beam [40–42].
- Drug delivery systems for chemotherapy (anti-cancer drug) and photo-dynamic therapy [43].
- Applications in advanced beam technologies (e.g. the laser cooling of electron beams [44]).

Because the above-mentioned large number of physics studies and advanced applications can be explored, recently many facilities have developed several types of LCS X/γ-ray sources such as a linac based system [2, 44–46] and an electron storage ring based system [47–49].

The proposed Shanghai Laser Electron Gamma Source (SLEGS) at the Shanghai Synchrotron Radiation Facility (SSRF) is an electron storage ring based system [50]. It will be built at beamline BL20 on one of the long straight sections of the SSRF storage ring and will be one of the highest intensity beam lines of γ-rays based on the LCS method using relativistic electron macropulses and a laser. The SLEGS will be used to conduct a wide range of fundamental studies (e.g., nuclear physics, particle physics, and astrophysics), and industrial and medical applications. According to our simulations, SLEGS is expected to generate a polarized γ-ray beam of up to 22 MeV and 10^9–10^{10} photons/s using a 3.5 GeV, 200–300 mA relativistic electrons of the SSRF storage ring and a 500 W polarized CO_2 laser in a backward laser-Compton scattering (BLCS) geometry. However, this design of the SLEGS does not allow for easy adjustment of the γ-ray energy because the energy of the 3.5 GeV electron bunch in the storage ring is fixed, and, as a result, many potential applications will be limited. So we propose to build an energy-tunable SLEGS by guiding of the laser incident angle from LCS. However, SLEGS has a low γ-ray flux for a slanting interaction because of a short interaction length [51]. In order to compensate the l oss of the γ-ray flux, we can employ a laser super-cavity to obtain a stacking laser pulse with a pulse energy gain of 10^2–10^3 and to realize a high-repetition collision rate [52].

A proof-of-principle experiment (SINAP I) [53] for the future SLEGS has been performed via Compton scattering of Q-switched Nd:YAG laser photons on ultrarelativistic electrons within the linear regime of the Compton scattering. Some evidence for LCS X-rays with the energies of 30 keV at the 2.5 sigma level was found. The SINAP II experiment was designed to further clarify the first experimental results and investigate the feasibility of energy-tunable photon source by guiding of laser incident angle from LCS. Originally we designed three laser incident angles of 40°, 90°, and 140°. Given the energy response of the Si(Li) detector used to detect the generated X-rays, we chose the laser incident angle of about 40° (44°) in this experiment.

The remainder of this paper consists of five sections. The next describes the principle of LCS. Sections 3 and 4 describe the arrangement of the LCS experiment with the 44°-configuration. Section 5 reviews the measured LCS X-ray results. Section 6 summarizes the experiment and the future outlook of the project.

2 Principle of the laser–Compton scattering

The interaction via laser–Compton scattering (LCS) is mainly approached in two ways: particle-particle interaction and the radiation of electrons in the electromagnetic field of the laser. In particle-particle interaction the collision between an electron and a laser photon is an elastic collision with conservation of energy and momentum during the collision. In the radiation of electrons, the dimensionless laser strength parameter a_0 plays an important role in determining the character of the emitted radiation. $a_0 = eA_0/m_e c^2$ is the normalized amplitude of the vector potential of the incident laser field. It can also be expressed by [54]

$$a_0 = 0.85 \times 10^{-9} \lambda_0 \sqrt{I_0}, \tag{1}$$

where λ_0 is the laser wavelength in µm and I_0 is the laser intensity in W/cm^2. As $a_0 \le 1$, the scattering occurs in the linear regime. Doppler-upshifted radiation is generated. At $a_0 \gg 1$ the non-linear regime is entered and some higher harmonics become visible. In our case, the laser pulses used for the interaction carry the energy of 0.9 J/pulse, are 8 ns long, and have the wavelength of 1064 nm (Nd:YAG). They can be focused to a spot of 200-µm radius at the interaction point with $a_0 \approx 0.0005$. Thus our experiment is in the linear LCS regime.

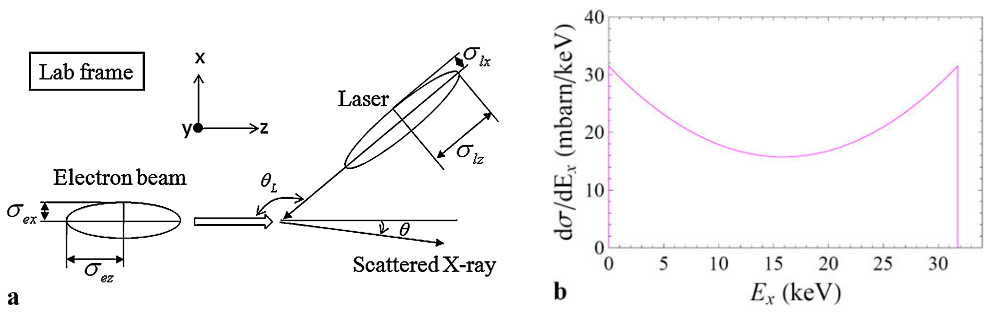

Fig. 1 **a** The coordinates for LCS between a relativistic electron and laser photon in the laboratory frame. **b** The scattered X-ray energy spectrum from Compton scattering. The parameters of laser and electron beams are shown in Table 1

The energy of the scattered X-ray depends on the energy of the electrons, the wavelength of the laser, and the laser incident and X-ray scattered angles. The parameters for LCS between a relativistic electron and a laser photon in the laboratory frame and the expected X-ray energy spectrum are shown in Fig. 1. The energy of the scattered X-ray photon is

$$E_x = E_{\mathrm{L}} \frac{(1-\beta\cos\theta_{\mathrm{L}})}{1-\beta\cos\theta + \frac{E_{\mathrm{L}}}{E_{\mathrm{e}}}[1-\cos(\theta_{\mathrm{L}}-\theta)]}, \qquad (2)$$

where β is the electron velocity normalized to the speed of light and equal to $1-(2\gamma^2)^{-1}$ for $\gamma \gg 1$ (γ is the total electron energy normalized to its rest energy), E_{e} and E_{L} are the energies of the incident electron and laser photon, and θ_{L} and θ are the incident angles of the laser photon and the scattered X-ray photon with respect to the direction of the incident electron beam. Typically, the energy of the incident photon is much lower than the energy of the electron, and therefore the X-rays are scattered in a small angle along the direction of the electron beam ($\theta \sim 1/\gamma$, where γ is the Lorentz factor).

The differential Compton scattering cross section comes from the Klein–Nishina formula and can be easily derived in the laboratory frame. It is [55, 56]

$$\frac{d\sigma}{d\Omega} = \frac{r_0^2}{2}\frac{1-\beta^2}{(1-\beta\cos\theta)^2}R^2\left[R+\frac{1}{R}-1+\cos^2\theta'\right], \qquad (3)$$

where r_0 is the classical radius of the electron, R is the ratio between the energies of scattered and incident photons with its value of $1/[1+(1+\cos\theta')(1+\beta)\gamma E_{\mathrm{L}}/m_0c^2]$, and $\cos\theta' = (\cos\theta-\beta)/(1-\beta\cos\theta)$. We calculate the total LCS cross section for our experiment in a cone of angle $\theta \sim 1/\gamma$ to be 400 mb.

Using (3), the total LCS X-ray yield for each collision between a laser pulse and a relativistic electron macropulse N_x can be estimated using

$$N_x = \sigma L, \qquad (4)$$

where L is the luminosity as determined by the collision geometry between the electron macropulse and the laser pulse. In the case of the collision between a laser pulse and an electron macropulse with a Gaussian spatial distribution, the luminosity L for an incident angle θ_{L} is [57]

$$L = \frac{N_{\mathrm{e}}N_{\mathrm{L}}(1-\beta\cos\theta_{\mathrm{L}})}{2\pi\sqrt{\sigma_{\mathrm{ey}}^2+\sigma_{\mathrm{ly}}^2}\sqrt{\sigma_{\mathrm{lx}}^2(1-\beta\cos\theta_{\mathrm{L}})^2+\sigma_{\mathrm{ex}}^2(\beta-\cos\theta_{\mathrm{L}})^2+\sigma_{\mathrm{lz}}^2\beta^2\sin^2\theta_{\mathrm{L}}+\sigma_{\mathrm{ez}}^2\sin^2\theta_{\mathrm{L}}}}, \qquad (5)$$

where N_{e} is the number of electrons in the electron macropulse and N_{L} is the number of photons in the laser pulse. The subscripts e and l refer to electron and laser; σ_x, σ_y and σ_z are the horizontal, vertical, and longitudinal rms sizes, respectively. Therefore, the cross section of the total LCS X-ray yield, $dN_x/d\Omega$, from (3) and (4) is

$$dN_x/d\Omega = L\,d\sigma/d\Omega. \qquad (6)$$

Considering the time jitter between the laser pulse and the electron macropulse, τ^{jitter}, the average of N_x for each collision, $\overline{N_x}$, and its standard deviation, $\sigma_{\overline{N_x}}$, are [51]

$$\overline{N_x} = N_x/\sqrt{\alpha^2+1} \qquad (7)$$

and

$$\sigma_{\overline{N_x}} = N_x\sqrt{\frac{1}{\sqrt{2\alpha^2+1}}-\frac{1}{\alpha^2+1}}, \qquad (8)$$

where the normalized time jitter $\alpha \equiv \tau^{\mathrm{jitter}}/\tau_0$, and

$$\tau_0 \equiv \sqrt{\sigma_{\mathrm{l}x}^2(1-\beta\cos\theta_{\mathrm{L}})^2+\sigma_{\mathrm{e}x}^2(\beta-\cos\theta_{\mathrm{L}})^2+(\sigma_{lz}\beta\sin\theta_{\mathrm{L}})^2+(\sigma_{\mathrm{ez}}\sin\theta_{\mathrm{L}})^2}/c.$$

Using (7) and (8), the number of the scattered X-ray photons, N_x', and its standard deviation, $\sigma_{N_x'}$, as functions of the time difference between the laser pulse and the electron macropulse are

$$N_x' = \overline{N_x}\exp\left[-\frac{1}{2}\left(\frac{t}{\overline{\tau}}\right)^2\right] \tag{9}$$

and

$$\sigma_{N_x'} = \sigma_{\overline{N_x}}\exp\left[-\frac{1}{2}\left(\frac{t}{\overline{\tau}}\right)^2\right], \tag{10}$$

where $\overline{\tau} \equiv \sqrt{\tau_0^2+(\tau^{\text{jitter}})^2}$.

3 Experimental description

Figure 2 shows the general setup of the experiment, which mainly contains a 100-MeV LINAC, a laser optical system, a LCS chamber, and an X-ray detection system. Each electron macropulse contains three micropulses and carries the total charge of 26.5 pC. The macropulses are generated at the repetition rate of 1–20 Hz by a thermionic cathode electron gun. The 100-MeV LINAC can provide an electron macropulse charge of ∼1.2 nC but we reduced the electron macropulse charge to 26.5 pC for measuring the LCS X-ray energy spectrum to avoid overflow and saturation of the detector due to the bremsstrahlung background radiation. The electron beam going through the center of the LCS chamber has been accelerated up to 112 MeV with four accelerating tubes and focused with quadrupole magnets. The electron beam position at the interaction point can be adjusted by steering magnets combined with the quadrupole magnets. After passing through the interaction point, the electron beam is deflected by a 30° bending dipole magnet and then separated from the forward scattered X-rays. Finally, the electron is absorbed in a Faraday dump housed in a lead enclosure.

The Nd:YAG laser (Beamtech, SGR-20) emitting pulses of 8-ns duration and 2-J energy is used as the incident photon source for the LCS experiment. The basic parameters of the Nd:YAG laser and the electron beam are summarized in Table 1. The Nd:YAG laser pulse with a repetition rate of 2.5 Hz passes through a beam expander, a beam splitter, several mirrors, and then propagates about 15 m to the final focusing optics with a focal length of 14.8 cm. It passes through a glass window and enters the LCS chamber at an incident angle of about 44° with respect to the electron beam axis. The photon loss through the whole transport is roughly 57%, leaving 860 mJ available at the interaction point. A He–Ne laser at the bottom of Fig. 2 is used to align the whole laser optical system. In addition, an energy and power meter sensor (EPM-1000) placed about 30 cm away from the beam splitter is used to measure the energy of some of the photons reflected by the beam splitter for monitoring the stability of the laser energy. A pin-photo diode detector near the EPM-1000 is used to determine the width of the Nd:YAG laser pulse and especially to monitor the arrival time of the laser pulse by measuring the other part of the reflected photons.

The generated X-rays from LCS pass through a 200-µm thick beryllium (Be) window, a 7-mm width lead slit, 7.8 m

Table 1 Summary of parameters of the electron beam and the Nd:YAG laser used in the experiment

Electron macropulse	
Number of micropulses	3
Separation of micropulses	∼350 ps
Electron energy	112 MeV
Macropulse total charge	26.5 pC/pulse
Normalized emittance (rms)[a]	60 mm mrad
Energy spread (rms)[a]	5‰
Pulse length (rms)	0.9 ns
Repetition rate	5 Hz
Spot size (standard deviation)	
Horizontal ($\sigma_{\mathrm{e}x}$)	1.5 mm
Vertical ($\sigma_{\mathrm{e}y}$)	1.9 mm
Nd: YAG laser	
Fundamental Wavelength	1064 nm
Energy at the interaction point	0.86 J/pulse
Pulse duration (FWHM)	7.8 ns
Repetition rate	2.5 Hz
Polarization	linear (in horizontal plane)
Spot size (standard deviation)	
Horizontal ($\sigma_{\mathrm{l}x}$)	<0.2 mm
Vertical ($\sigma_{\mathrm{l}y}$)	<0.2 mm
Laser incident angle[b]	44 ± 2°

[a] See Ref. [58]

[b] For the electron energy of 112 MeV and the laser wavelength of 1064 nm, the laser incident angle is determined to be 44° by (2), using the ending point of the LCS energy spectrum

Fig. 2 LCS experimental setup

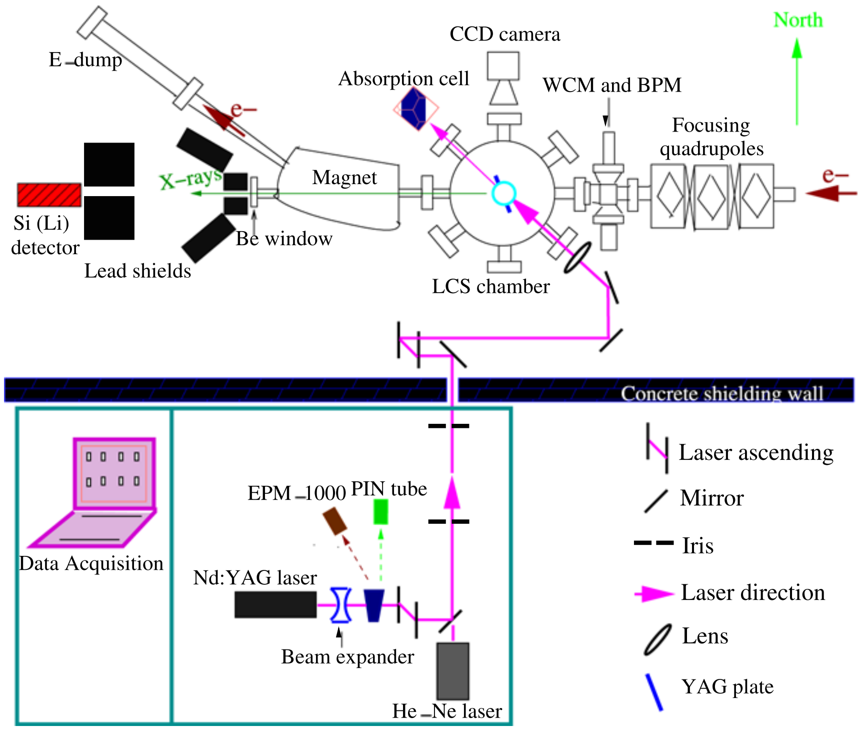

air, and a hollowed cylindrical lead collimator with an inner diameter of 6 mm and length of 60 mm before reaching the Si(Li) detector placed at 0° along the electron beam axis. The distance between the LCS chamber and detector is 9.8 m and the solid angle, $\Delta\Omega$, subtended by the detector is 0.29 µsr.

Compared with the first experiment (SINAP I), this one achieved three major technical and experimental improvements. The Nd:YAG laser and its optical system were upgraded. The peak-power is about 20 times higher and the pulse duration is 2.5 times shorter than the values in SINAP I [53]. In addition, a much smaller focal spot size at the interaction point was achieved resulting from enlarging the laser spot on the focusing optics. The lead slit was more precisely aligned: After SINAP I we had found that the center of the lead slit downstream the Be-window in Fig. 2 was misaligned by 3 mm along the electron beam axis. Position and time scans of the Si(Li) detector were performed to optimize the Si(Li) detector position and the LCS X-ray yield. We measured the generated LCS X-ray yield as a function of the time difference between the electron macropulse and the Nd:YAG laser pulse and the X-ray divergence angle (converted from the Si(Li) detector position). More details are presented in Sect. 5.

4 Alignments

Spatial overlap and synchronization between the Nd:YAG laser pulse and the electron macropulse is a key issue. With a YAG plate and a 16-bit charge-coupled device (CCD) camera, the spatial overlap of the focal spots of the laser pulse and the electron macropulse at the interaction point is measured. A He–Ne laser is used to facilitate the alignment of the Nd:YAG laser and the electron macropulse at the interaction point. This also helps avoiding damage caused when the high-power Nd:YAG laser hits the YAG plate and the camera directly. In the observed images, the electron beam and the He–Ne laser overlap well as shown in Fig. 3. The axes of the He–Ne laser and the Nd:YAG laser are well aligned: The position deviation between the He–Ne laser and the Nd:YAG laser at the center of the LCS chamber is less than 0.1 mm.

A synchronization diagram is shown in Fig. 4. There are three main steps to achieve synchronization. First, we measure and check carefully the Nd:YAG laser pulse and the electron macropulse jitter, pulse generator (M1 and M2) jitter, cable delay times, total length of optical path, and so on. The Nd:YAG laser pulse jitter, τ_l, is about 0.6 ns as measured by the pin-photo diode detector. The electron macropulse jitter, τ_e, is about 0.6 ns as measured by a wall current monitor (WCM). Considering peak-to-peak synchronization of the Nd:YAG laser pulse and the electron macropulse at the interaction point, the time difference is expected to be 158.3 ± 1.0 ns based on measurements. Second, we monitor the time difference (see Fig. 5) between the Nd:YAG laser pulse and the electron macropulse by an oscilloscope with the help of the pin-photo diode detector and the WCM. Finally, we perform a scan of the time difference between the Nd:YAG laser pulse and the electron macropulse by adjusting the delay time of M1 and M2. The

Fig. 3 Spot images of the electron beam (*left*) and the He–Ne laser beam (*right*) at the center of the LCS chamber (the interaction point) observed with the 16-bit CCD camera

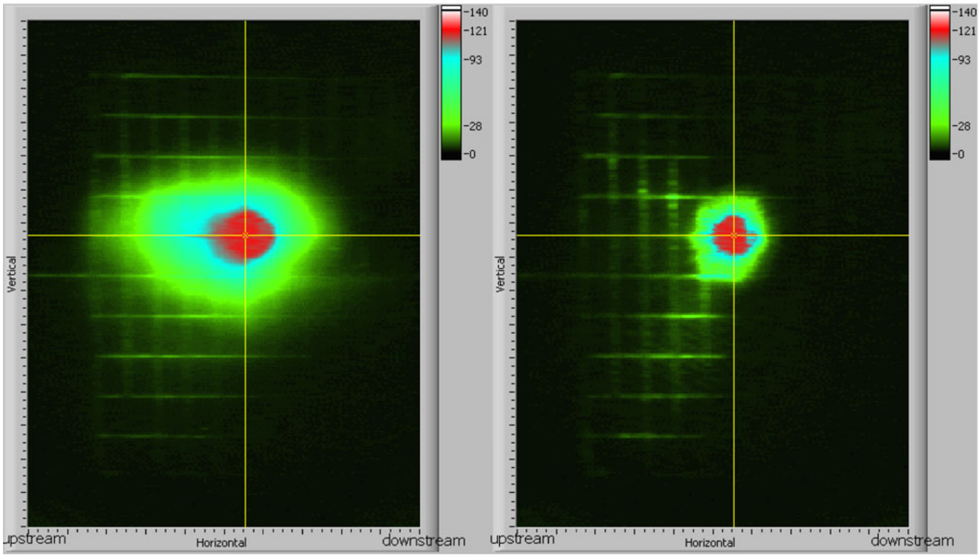

Fig. 4 Scheme for the synchronization of the Nd:YAG laser pulse and the electron macropulse. M1 and M2 are eight-channel programmable pulse-generators. M1 runs with the repetition of 5 Hz and provides several TTL trigger signals to the following devices: (1) Electron gun, (2) Nd:YAG laser, and (3) M2. M2 provides a pre-trigger signal to the Nd:YAG laser. The oscilloscope (TDS 7104) and its LabVIEW program are used to monitor and record the relative time difference between the laser pulse and the electron macropulse

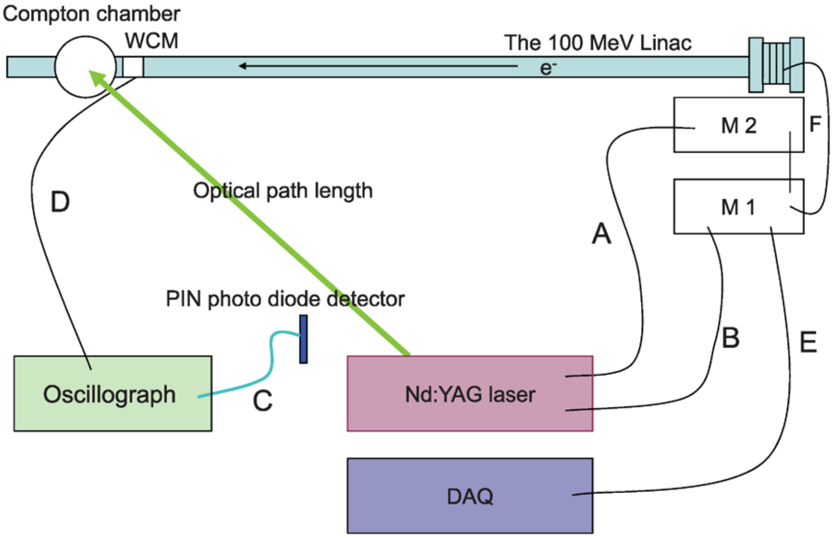

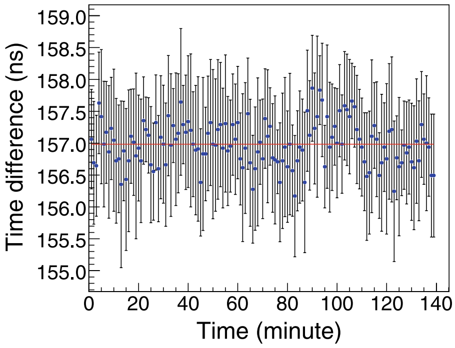

Fig. 5 Time difference between the Nd:YAG laser pulse and the electron macropulse measured by the oscilloscope. Each data point is a one-minute average. The error bars mainly arise from the systematic errors associated with the Nd:YAG laser pulse jitter, τ_1, and the electron macropulse jitter, τ_e. The *red line* is the average of the total time difference

synchronization between the Nd:YAG laser pulse and the electron macropulse at the interaction point can be established by adjusting the delay time of M1 and M2 to generate the maximum LCS X-ray yield.

Besides the synchronization and the spatial alignment, some other challenges have to be overcome, too, in particular the low signal-to-noise ratio (SNR) (extracting the LCS X-ray signal in presence of a low SNR) and the signal-photon detection (measuring the X-ray spectrum). How these issues are resolved is explained in detail in Ref. [53].

5 Experimental results and discussion

5.1 Scan of the X-ray divergence angle

We need to determine the Si(Li) detector position in order to detect the X-ray signals. There are two main steps to achieve

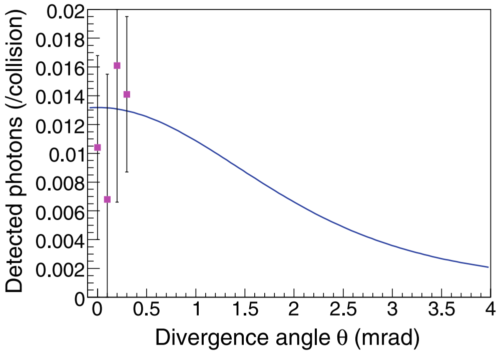

Fig. 6 The detected and theoretical LCS X-ray count rates as a function of the X-ray divergence angle (converted from the Si(Li) detector position)

the optimal Si(Li) detector position. The Si(Li) detector is first positioned where the total yield including background radiation and the generated X-rays is maximized. Second, the fine adjustment of the detector position is performed by scanning its position vertically or horizontally with a step of 1.0 mm around the initial position. The experimental LCS X-ray count rate, Y, with respect to the detector position is measured. The LCS X-ray yield per collision at the interaction point is

$$N_x^{\mathrm{exp}} = \frac{Y}{\gamma^2 \Delta\Omega \eta \xi \zeta}, \tag{11}$$

where γ is the electron relativistic factor equal to 219, $1/\gamma^2$ is the narrow solid angle of the generated LCS X-rays, $\Delta\Omega$ is the solid angle of the detector equal to 0.29 µsr, η is the total LCS X-ray transmission efficiency accounting for the transmissions of the 200-µm Be-window (99.4%) and the 7.8 m air path (77.3%), ξ is the idle efficiency of the Si(Li) detector equal to 30% in this LCS experiment, and ζ is the efficiency of the Data Acquisition system equal to 100% at 5 Hz. We found that the efficiency of the DAQ system is close to 100% when the detector count rate is less than 20 Hz. Therefore, based on N_x^{exp} the dependence of the LCS X-ray yield recorded by the Si(Li) detector on the X-ray divergence angle can be extracted. This dependence and the theoretical prediction from (6) are shown in Fig. 6 proving that the detected LCS X-ray photon yield is consistent with the theoretical prediction in the θ-range investigated experimentally.

5.2 Time scan for maximal LCS X-ray yield

The synchronization is initially achieved by setting the time difference between the Nd:YAG laser pulse and the electron macropulse to 158 ns as recorded by the oscilloscope (see Sect. 4). After the position of the Si(Li) detector is optimized, a time scan is performed by adjusting this time difference in steps of ∼1 ns around 158 ns. During the time scan, we measure the LCS X-ray yield per collision, N_x^{exp}, as a function of the time difference between the electron macropulse and the Nd:YAG laser pulse. The result is shown in Fig. 7.

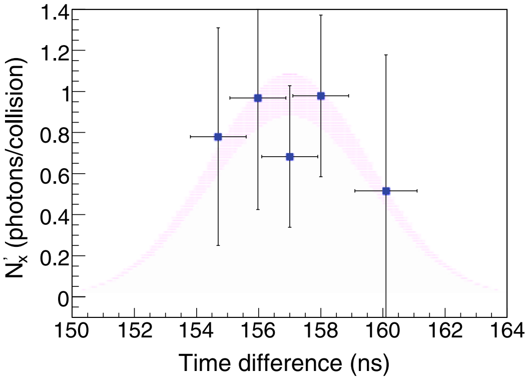

Fig. 7 The generated X-ray yield as a function of the time difference between the electron macropulse and the Nd:YAG laser pulse recorded by the oscilloscope. The *shaded band* is the theoretical estimation. The uncertainty of the LCS X-ray yield is due to the time jitter of 1.0 ns

Considering the peak-to-peak time jitter between the electron macropulse and the laser pulse of 1 ns, the theoretical estimation with its uncertainty of the LCS X-ray yield due to this time jitter is obtained from (9) and (10) and is also shown in Fig. 7. All parameters used in (9) and (10) are summarized in Table 1. The numbers of laser photons, N_{L} , and electrons, N_{e}, are calculated to be 4.82×10^{18} photons/pulse and 1.66×10^8 electrons/pulse from the laser pulse energy (0.86 J) and the electron macropulse charge (26.5 pC), respectively; the laser pulse duration (FWHM) of 7.8 ns corresponds to $\sigma_{\mathrm{l}z} = 1.0 \times 10^2$ cm; the longitudinal length of the electron macropulse of 0.9 ns corresponds to $\sigma_{\mathrm{e}z} = 25.5$ cm. Based on (4) and (5), the luminosity L and the average of the total LCS X-ray yield, $\overline{N_x}$, are 2.7×10^{28} m^{-2} and 1.0 photons/collision, respectively, where α is calculated to be 0.4. We conclude that the time difference between the laser pulse and the electron macropulse maximizing the LCS X-ray yield is between 156 ns and 158 ns, agreeing with our expectation of 158.3 ± 1.0 ns.

5.3 LCS X-ray energy spectrum and its flux

During this experiment, data is taken alternatively with laser pulse on and off. The Nd:YAG laser and the electron beam repetition rates are 2.5 Hz and 5 Hz, respectively. We use data with laser pulse on minus data with laser pulse off to separate the LCS X-ray signal from background radiation. Background radiation can be largely suppressed if the laser pulse and electron beam are stable. Although the SNR is very low in this experiment, the generated LCS X-rays can still be observed by this method; similar methods have been widely used in the measurement of small asymmetries

Table 2 The LCS experimental parameters including the generated LCS X-rays

Parameter	SINAP I	SINAP II
Electron beam		
Macropulse energy (MeV)	108	112
Macropulse charge (nC)	∼0.1 (1.0)	0.027 (1.0)
Pulse length (rms) (ns)	0.95	0.9
rms spot size at focus (σ_{ex}/σ_{ey}) (mm)	3.1/2.5	1.5/1.9
Nd: YAG laser		
Wavelength (nm)	1064	1064
Pulse energy (J)	0.113	0.9 (2.0)
Pulse duration (FWHM) (ns)	21	7.8
rms spot size at focus (σ_{1x}/σ_{1y}) (mm)	$<0.5/<0.5$	$<0.2/<0.2$
Laser incident angle	42°	44±2°
Relative time jitter at interaction point (ns)	1.3	1.0
X-rays		
Peak energy (keV)	$29.1 \pm 4.4_{\rm stat} \pm 2.1_{\rm syst}$	$31.73 \pm 0.22_{\rm stat} \pm 1.64_{\rm syst}$
Peak width (keV)	$7.8 \pm 2.8_{\rm stat} \pm 0.4_{\rm syst}$	$0.74 \pm 0.26_{\rm stat} \pm 0.03_{\rm syst}$
Photons/s (total spectrum)[a]	$(5.2 \pm 2.0) \times 10^2$	$(1.7 \pm 0.3) \times 10^3$

[a] X-ray flux (total spectrum) from SINAP I and II normalized to an electron macropulse carrying the charge of 1 nC

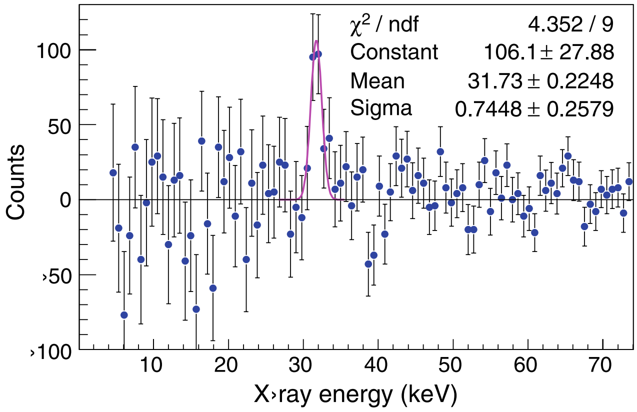

Fig. 8 The LCS X-rays energy spectrum after background subtraction

in spin physics: asymmetries as small as 10^{-8} were measured [59].

The LCS X-ray energy spectrum obtained after background subtraction is shown in Fig. 8. The horizontal axis is inscribed with the energy of a single photon whose energy is calibrated by the standard X-ray sources from ^{125}I and ^{55}Fe radioactive sources. By fitting the LCS X-ray energy spectrum, the peak energy and the peak width of the LCS X-ray spectrum are $31.73 \pm 0.22_{\rm stat} \pm 1.64_{\rm syst}$ keV and $0.74 \pm 0.26_{\rm stat} \pm 0.03_{\rm syst}$ keV. Here the subscripts *stat* and *syst* refer to statistical and systematic errors. In order to compare with SINAP I [53], the LCS experimental conditions and their results including the observed LCS X-ray peak energies and widths are compiled in Table 2. The measured peak energy is consistent with that in SINAP I.

The LCS X-ray flux is obtained from the LCS X-ray yield per collision, $N_x^{\rm exp}$, at the interaction point, which is 0.92 ± 0.16 photons/collision from (11) for an electron macropulse charge of 26.5 pC and the laser pulse energy of 0.9 J. Normally the 100-MeV LINAC operates with the electron macropulse charge of 1.0–1.2 nC/pulse, an incident laser pulse energy of 2 J, and an electron and laser collision repetition rate of 20 Hz. The corresponding LCS X-ray flux is listed in the right-hand column in Table 2 as $(1.7 \pm 0.3) \times 10^3$ photons/s from $N_x^{\rm exp}$. When increasing the electron beam current from 26.5 pC/macropulse to 1.0 nC/macropulse, it has to be realized that other properties of the electron beam are changed, too. For example, the electron beam emittance due to the space charge effect will grow. Therefore the X-ray flux as given above is only a rough estimate.

6 Summary and outlook

We have demonstrated the generation of quasi-monochromatic laser-Compton scattering X-rays with a peak energy of about 30 keV by the interaction of Q-switched Nd:YAG laser pulses (wavelength 1064 nm, pulse width 8 ns, and pulse energy 2 J) and electron macropulses (energy 112 MeV and pulse width 0.9 ns (rms)) at the angle of 44°. The generated X-ray peak is visible and its peak energy is consistent with that in SINAP I. The LCS X-ray yield as a function of the time difference between the electron macropulse and the laser pulse and the angular distribution of the detected LCS X-ray count rates with

Table 3 Typical parameters of laser, electron beam and γ-rays at the future SLEGS

Electron in storage ring		
Electron energy	GeV	3.5
Bunch intensity (single/multi bunch)	mA	$5/200 \sim 300$
Bunch length (σ_{ez})	mm	4
RMS beam size (σ_{ex})	µm	30–40
RMS beam size (σ_{ey})	µm	50–60
Normalized emittance	nm rad	3.9
Nd:YAG laser		
Wavelength	nm	1064
Peak power	GW	10
RMS beam size (σ_{lx})	µm	50
RMS beam size (σ_{ly})	µm	50
Pulse length (σ_{lz})	ps	10
Laser incident angle		10°–170°
Gain of laser super-cavity		10–100
γ-rays		
Peak energy adjustable	MeV	1.6–204
Flux (two orders energy gain is considered)	Photons/s	1.9×10^9–2.4×10^{11}

the X-ray scattered angle are presented. Normally, the 100-MeV LINAC operates with an electron macropulse charge of 1.0 nC/pulse, an incident laser pulse energy of 2 J, and an electron and laser collision repetition rate of 20 Hz. Therefore, a total LCS X-ray flux of $(1.7 \pm 0.3) \times 10^3$ photons/s can be achieved.

This experiment is the foundation for two future applications. Based on (4) and (5), we simulate the γ-ray features for the future SLEGS. A conventional GW and ps Nd:YAG laser and a laser super-cavity with an energy gain of 100 are employed in our simulation. More detailed parameters of the laser and electron beams are summarized in Table 3. The future SLEGS can be a high flux (1.9×10^9–2.4×10^{11} photons/s) and energy-tunable (1.6–204 MeV) γ-ray source according to our simulation. However, there will be many technical difficulties and challenges for constructing energy-tunable SLEGS, e.g. building a laser super-cavity with a high gain. Also the generation of high flux γ-rays may affect the electron lifetime in the storage ring and the performance of the SSRF [60]. So we are going to construct the SLEGS with a low photon flux first and (if possible) then update it **s** flux to about 10^{10} photons/s using a laser super-cavity. Based on the experimental device, we design the future SINAP III. If an updated terawatt and fs Ti: Sapphire laser and the layout of backward LCS are employed, SINAP III will become an X/γ-ray source with a flux of 10^6–10^8 photons/s and a pulse length from ps down to hundreds of fs. This source will be of great interest for the study of the interaction between ultra-intense laser and electron beams (e.g. laser acceleration of electrons, non-linear laser–Compton scattering, and radiation damping), and in many other fields, e.g., non-destructive assay of radioactive nuclides and detection and management of nuclear waste in nuclear research and industry [61, 62].

Acknowledgements We would like to thank the staff of the 100-MeV LINAC at SINAP for operating the LINAC. This work is supported by One Hundred Talents Project of Chinese Academy of Sciences (2006) (26010701), by Knowledge Innovation Project of Chinese Academy of Sciences (KJCX2-SW-N13), by Pujiang Talent Project of the Shanghai Science and Technology Committee (06PJ14114), and by the National Natural Science Foundation of China (10675156).

References

1. A. D'Angelo, O. Bartalini, V. Bellini, P. Levi Sandri, D. Moricciani, L. Nicoletti, A. Zucchiatti, Nucl. Instrum. Methods A **455**, 1 (2000)
2. K. Chouffani, D. Wells, F. Harmon, J. Jones, G. Lancaster, Nucl. Instrum. Methods A **495**, 95 (2002)
3. V.N. Litvinenko, B. Burnham, M. Emamian, N. Hower, J.M.J. Madey, P. Morcombe, P.G. O'Shea, S.H. Park, R. Sachtschale, K.D. Straub, G. Swift, P. Wang, Y. Wu, Phys. Rev. Lett. **78**, 4569 (1997)
4. D. Li, K. Imasaki, M. Aoki, S. Miyamoto, S. Amano, K. Aoki, K. Hosono, T. Mochizuki, Nucl. Instrum. Methods A **528**, 516 (2004)
5. H. Ohgaki, S. Sugiyama, T. Yamazaki, T. Mikado, M. Chiwaki, K. Yamada, R. Suzuki, T. Noguchi, T. Tomimasu, IEEE Trans. Nucl. Sci. **38**, 386 (1991)
6. T. Nakano, J.K. Ahn, M. Fujiwara, H. Kohri, N. Matsuoka, T. Mibe, N. Muramatsu, M. Nomachi, H. Shimizu, K. Yonehara, M. Yosoi, T. Yorita, W.C. Chang, C.W. Wang, S.C. Wang, Y. Asano, T. Hotta, Y. Sugaya, R. Zegers, S. Daté, N. Kumagai, Y. Ohashi, H. Ohkuma, H. Toyokawa, T. Iwata, M. Miyabe, Y. Miyachi, A. Wakai, K. Imai, T. Ishikawa, M. Miyabe, T. Sasaki, H. Kawai, T. Ooba, Y. Shiino, M. Wada, H. C Bhang, Z.Y. Kim,

A. Sakaguchi, M. Sumihama, K. Hicks, H. Akimune, T. Matsumura, C. Rangacharvulu, S. Makino, Nucl. Phys. A **684**, 71c (2001)

7. K. Kawase, Y. Arimoto, M. Fujiwara, S. Okajima, M. Shoji, S. Suzuki, K. Tamura, T. Yorita, H. Ohkuma, Nucl. Instrum. Methods A **592**, 154 (2008)
8. D.J. Gibson, S.G. Anderson, C.P.J. Barty, S.M. Betts, R. Booth, W.J. Brown, J.K. Crane, R.R. Cross, D.N. Fittinghoff, F.V. Haremann, J. Kuba, G.P. Le Sage, D.R. Slaughter, P.T. Springer, Phys. Plasmas **11**, 2857 (2004)
9. M. Babzien, I. Ben-Zvi, K. Kusche, I.V. Pavlishin, I.V. Pogorelsky, D.P. Siddons, V. Yakimenko, D. Cline, F. Zhou, T. Hirose, Y. Kamiya, T. Kumita, T. Omori, J. Urakawa, K. Yokoya, Phys. Rev. Lett. **96**, 054802 (2006)
10. T. Kawachi, M. Kado, M. Tanaka, A. Sasaki, N. Hasegawa, A.V. Kilpio, S. Namba, K. Nagashima, P. Lu, K. Takahashi, H. Tang, R. Tai, M. Kishimoto, M. Koike, H. Daido, Y. Kato, Phys. Rev. A **66**, 033815 (2002)
11. A. Endo, Proc. SPIE **5063**, 269 (2003)
12. http://www.tunl.duke.edu/higs/review/
13. T. Kawachi, M. Kado, M. Tanaka, A. Sasaki, N. Hasegawa, A.V. Kilpio, S. Namba, K. Nagashima, P. Lu, K. Takahashi, H. Tang, R. Tai, M. Kishimoto, M. Koike, H. Daido, Y. Kato, Phys. Rev. Lett. **100**, 162502 (2008)
14. S. Goko, H. Utsunomiya, S. Goriely, A. Makinaga, T. Kaihori, S. Hohara, H. Akimune, T. Yamagata, Y.-W. Lui, H. Toyokawa, A.J. Koning, S. Hilaire, Phys. Rev. Lett. **96**, 192501 (2006)
15. H. Ohgaki, H. Toyokawa, K. Kubo, N. Takeda, T. Yamazaki, Nucl. Instrum. Methods A **455**, 54 (2006)
16. T. Shima, S. Naito, Y. Nagai, T. Baba, K. Tamura, T. Takahashi, T. Kii, H. Ohgaki, H. Toyokawa, Phys. Rev. C **72**, 044004 (2005)
17. H. Harada, F. Kitatani, S. Goko, K.Y. Hara, H. Toyokawa, T. Kaihori, H. Ustunomiya, J. Nucl. Sci. Technol. **45**, 1228 (2008)
18. T. Omori, T. Aoki, K. Dobashi, T. Hirose, Y. Kurihara, T. Okugi, I. Sakai, A. Tsunemi, J. Urakawa, M. Washio, K. Yokoya, Nucl. Instrum. Methods A **500**, 232 (2003)
19. I. Watanabe, S. Hiramatsu, K. Nakajima, T. Tauchi, K. Yokoya, I. Endo, K. Matsukado, T. Ohgaki, T. Takahashi, I. Ito, T. Kon, N. Matsuda, T. Takeshita, $\gamma\gamma$ collider as an option of JLC. KEK Report 97-17, 1998
20. Zeroth order design report for the next linear collider, SLAC-474, 1996
21. Physics and technology of the next linear collider, SLAC Report 485, 1996
22. R. Brinkmann, I. Ginzburg, N. Holtkamp, G. Jikia, O. Napoly, E. Saldin, E. Schneidmiller, V. Serbo, G. Silvestrov, V. Telnov, A. Undrus, M. Yurkov, Nucl. Instrum. Methods A **406**, 13 (1998)
23. V.I. Telnov, Nucl. Instrum. Methods A **294**, 72 (1990)
24. C.E. Clayton, N.A. Kurnit, D.D. Meyerhofer, Nucl. Instrum. Methods A **355**, 121 (1995)
25. F.E. Carroll, M.H. Mendenhall, R.H. Traeger, C. Brau, J.W. Waters, Am. J. Roentgenol. **181**, 1197 (2003)
26. R. Kuroda, H. Toyokawa, N. Sei, M. Yasumoto, H. Ogawa, M. Koike, K. Yamada, T. Nakajyo, F. Sakai, T. Yanagida, Int. J. Mod. Phys. B **21**, 488 (2007)
27. H. Ikeura-Sekiguchi, R. Kuroda, M. Yasumoto, H. Toyokawa, M. Koike, K. Yamada, F. Sakai, K. Mori, K. Maruyama, H. Oka, T. Kimata, Appl. Phys. Lett. **92**, 131107 (2008)
28. K. Yamada, R. Kuroda, H. Toyokawa, H. Ikeura-Sekiguchi, M. Yasumota, N. Sei, H. Ogawa, M. Koike, R. Suzuki, F. Sakai, K. Mori, H. Mori, N. Fukuyama, E. Sato, in *Proc. ICFA Workshop on "Compton Sources for X/gamma Rays: Physics and Applications*", Alghero, Italy, September 2008
29. H. Toylkawa, Nucl. Instrum. Methods A **545**, 469 (2005)
30. S. Miyamoto, Y. Asano, S. Amano, D. Li, K. Imasaki, H. Kinugasa, Y. Shoji, T. Takagi, T. Mochizuki, Radiat. Meas. **41**, S179 (2007)
31. N. Kikuzawa, R. Hajima, N. Nishimori, E. Minehara, T. Hayakawa, T. Shizuma, H. Toyokawa, H. Ohgaki, Appl. Phys. Express **2**, 036502 (2009)
32. R. Hajima, T. Hayakawa, N. Kikuzawa, E. Minehara, J. Nucl. Sci. Tech. **45**, 441 (2008)
33. D. Li, K. Imasaki, M. Aoki, S. Miyamoto, S. Amano, K. Aoki, K. Hosono, T. Mochizuki, Nucl. Instrum. Methods A **528**, 516 (2004)
34. J. Pruet, D.P. McNabb, C.A. Hagmann, F.V. Hartemann, C.P.J. Barty, J. Appl. Phys. **99**, 123102 (2006)
35. R. Hajima, N. Kikuzawa, N. Nishimori, T. Hayakawa, T. Shizuma, K. Kawase, M. Kando, E. Minehara, H. Toyokawa, H. Ohgaki, Nucl. Instrum. Methods A **608**, S57 (2009)
36. D. Attwood, *Soft X-rays and Extreme Ultraviolet Radiation: Principles and Applications* (Cambridge University Press, Cambridge, 1999)
37. R.W. Schoenlein, W.P. Leemans, A.H. Chin, P. Volfbeyn, T.E. Glover, P. Balling, M. Zolotorev, K.-J. Kim, S. Chattopadhyay, C.V. Shank, Science **274**, 236 (1996)
38. C.J. Joshi, P.B. Corkum, Phys. Today **48**, 36 (1995)
39. W.P. Leemans, R.W. Schoenlein, P. Volfbeyn, A.H. Chin, T.E. Glover, P. Balling, M. Zolotorev, K.-J. Kim, S. Chattopadhyay, C.V. Shank, IEEE J. Quantum Electron. **33**, 1925 (1997)
40. B. Girolami, B. Larsson, M. Preger, C. Schaerf, J. Stepanek, Phys. Med. Biol. **41**, 1581 (1996)
41. K.J. Weeks, Nucl. Instrum. Methods A **393**, 544 (1997)
42. K.J. Weeks, V.N. Litvinenko, J.M.J. Madey, Med. Phys. **24**, 417 (1997)
43. A. Harada, K. Kataoka, Science **283**, 65 (1999)
44. V. Telnov, Phys. Rev. Lett. **78**, 4757 (1997)
45. G. Priebe, D. Laundy, M.A. Macdonald, G.P. Diakun, S.P. Jamison, L.B. Jones, D.J. Holder, S.L. Smith, P.J. Phillips, B.D. Fell, B. Sheehy, N. Naumova, I.V. Sokolov, S. Ter-Avetisyan, K. Spohr, G.A. Krafft, J.B. Rosenzweig, U. Schramm, F. Grüner, G.J. Hirst, J. Collier, S. Chattopadhyay, E.A. Seddon, Laser Part. Beams **26**(04), 649 (2008). doi:10.1017/S0263034608000700
46. R. Hajima, N. Kikuzawa, N. Nishimori, T. Hayakawa, E. Minehara, T. Shizuma, K. Kawase, M. Kando, H. Toyokawa, H. Ohgaki, in *Proc. ICFA Workshop on "Compton Sources for X/gamma Rays: Physics and Applications"*, Alghero, Italy, September 2008
47. http://www.tunl.duke.edu/higs
48. V. Androsov, A. Agafonov, J.I.M. Botman, E. Bulyak, I. Drebot, P. Gladkikh, V. Grevtsev, V. Ivashchenko, I. Karnaukhov, V. Lapshin, A. Lebedev, V. Markov, N. Mocheshnikov, A. Mytsykov, F. Peev, A. Ryezayev, A. Shcherbakov, V. Skomorokhov, V. Skyrda, R. Tatchyn, Y. Telegin, V. Trotsenko, A. Zelinsky, Nucl. Instrum. Methods A **543**, 58 (2005)
49. R. Ruth, J. Rifkin, L. Roderick, in *Proc. ICFA Workshop on "Compton Sources for X/gamma Rays: Physics and Applications"*, Alghero, Italy, September 2008
50. Q.Y. Pan, W. Xu, W. Luo, X.Z. Cai, J.G. Chen, G.T. Fan, G.W. Fan, W. Guo, Y.J. Li, G.Q. Lin, Y.G. Ma, W.Q. Shen, X.C. Shi, H.W. Wang, B.J. Xu, J.Q. Xu, Y. Xu, Z. Yan, L.F. Yang, M.H. Zhao, Synchrotron Radiat. News **22**, 11 (2009)
51. M. Yorozu, J. Yang, Y. Okada, T. Yanagida, F. Sakai, K. Takasago, S. Ito, A. Endo, Appl. Phys. B **74**, 327 (2002)
52. J. Urakawa, in *Proc. ICFA Workshop on "Compton Sources for X/gamma Rays: Physics and Applications"*, Alghero, Italy, September 2008
53. W. Luo, W. Xu, Q.Y. Pan, X.Z. Cai, J.G. Chen, Y.Z. Chen, G.T. Fan, G.W. Fan, W. Guo, Y.J. Li, W.H. Liu, G.Q. Lin, Y.G. Ma, W.Q. Shen, X.C. Shi, B.J. Xu, J.Q. Xu, Y. Xu, H.O. Zhang, Z. Yan, L.F. Yang, M.H. Zhao, Rev. Sci. Instrum. **81**, 013304 (2010)
54. S.K. Ride, E. Esarey, M. Baine, Phys. Rev. E **52**, 5245 (1995)
55. O. Klein, Y. Nishina, Z. Phys. **52**, 853 (1929)

56. J. Stepaneck, Nucl. Instrum. Methods A **412**, 174 (1998)
57. S. Kashiwagi, R. Kuroda, T. Oshima, F. Nagasawa, T. Kobuki, D. Ueyama, Y. Hama, M. Washio, K. Ushida, H. Hayano, J. Urakawa, J. Appl. Phys. **98**, 123302 (2005)
58. Z.T. Zhao, Report of OCPA Topical Accelerator School & Workshop in Beijing, China, August 2009 (unpublished)
59. J.M. Potter, J.D. Bowman, C.F. Hwang, J.L. McKibben, R.E. Mischke, D.E. Nagle, P.G. Debrunner, H. Frauenfelder, L.B. Sorensen, Phys. Rev. Lett. **33**, 1307 (1974)
60. H. Toyokawa, S. Goko, S. Hohara, T. Kaihori, F. Kaneko, R. Kuroda, N. Oshima, M. Tanaka, M. Koike, A. Kinomura, H. Ogawa, N. Sei, R. Suzuki, T. Ohdaira, K. Yamaka, H. Ohgaki, Nucl. Instrum. Methods A **608**, S41 (2009)
61. N. Kikuzawa, R. Hajima, N. Nishimori, E. Minehara, T. Hayakawa, T. Shizuma, H. Toyokawa, H. Ohgaki, Appl. Phys. Express **2**, 036502 (2009)
62. J. Pruet, D.P. McNabb, C.A. Hagmann, F.V. Hartemann, C.P.J. Barth, J. Appl. Phys. **99**, 123102 (2006)